Harmonic transition state theory applied to vacancy diffusion pre-exponential factors in a concentrated solid-solution alloy

Joseph Lefèvre López [1], Normand Mousseau [1], Gilles Adjanor [2], and Christophe Domain [2]

[1] *Département de Physique and Regroupement Québécois sur les Matériaux de Pointe, Université de Montréal, Case Postale 6128, Succursale Centre-ville, Montréal, Québec H3C 3J7, Canada*

[2] *Electricité de France, EDF Recherche et Développement, Département Matériaux et Mécanique des Composants, Les Renardières, F-77250 Moret sur Loing, France*

(Received 6 April 2023; accepted 28 November 2023; published 30 January 2024)

High-entropy alloys are solid solutions composed of five or more elements in near-equimolar proportions that demonstrate a number of unusual properties that have yet to be fully explained. Among these, the origin and existence of diffusion qualified as sluggish have been debated since the first measurements of diffusion in disordered systems became available. To better understand the potential role of entropy in this phenomenon, we analyze vacancy diffusion in a ternary concentrated solid-solution alloy, FeNiCr. This is done through atomistic simulations using the kinetic activation-relaxation technique, an off-lattice kinetic Monte Carlo algorithm combined with an embedded atom method potential. Through an analysis of millions of activated events, we compare the kinetics of a vacancy when the activation prefactor is computed specifically within the harmonic approximation to a system where activated prefactors are set at a constant value, regardless of the environment. This allows us to identify the role of disorder on energetic barriers and prefactor distributions, particularly in the case of defect kinetics. More precisely, through the emerging statistical evidence of a compensation between the barrier and prefactor, we show that disorder strongly perturbs the system's vibrational entropy, contributing to explain sluggish diffusion.

DOI: 10.1103/PhysRevMaterials.8.013609

I. INTRODUCTION

High entropy alloys (HEAs) are metastable solid-solutions composed of five or more elements in near equimolar proportions randomly placed on the crystalline lattice sites. Such metallic alloys have received considerable attention due to a number of interesting properties [1–3], including a decrease in the shear modulus with an increase of point defect concentration [4], a high-temperature strength [3,5,6], and indications of a potentially high resistance to neutron radiation damage [7–10] that make some of these alloys appealing in high-temperature applications.

In addition to these, the sluggish diffusion in HEAs, proposed as one of the four core effects by Yeh *et al.* in 2004 [5], has since been subject of considerable debate. Although this phenomenon has often been used to explain their strength and stability at high temperature [2,11,12], this characteristic is difficult to measure and analyze experimentally: Since the diffusion rate in an alloy is obtained through secondary observations of the system's kinetics, measurements do not necessarily prove the presence of sluggish diffusion [13]. Moreover, recent observation of a case of nonsluggish diffusion of Zr in HfTiZrNbTa and HfTiZrNbV by Zhang *et al.* suggests that sluggish diffusion might not be an inherent property of HEAs [14].

To shed light on fundamental properties linked to this diffusion, we turn to atomistic off-lattice kinetic Monte Carlo (KMC) simulations of concentrated solid-solution alloys (CSAs). These metastable alloys [15] contain fewer elements in more variable proportions but show similar high-temperature properties, such as a high radiation damage resistance [16,17]. Even if it has been shown that diffusion tends to slow down as the number of elements in the alloy increases, a study of the defect kinetics in a simpler CSA allows us to better grasp the role of vibrational entropy in this phenomenon. We focus here on the effect of the activated diffusion prefactor on the overall vacancy diffusion. While standard lattice-based KMC modeling tends to use a fix prefactor in computing event rates [18], recent work showed that, in some disordered materials, the prefactor could vary by orders of magnitude for similar energy barriers [19–21].

Indeed, in previous work [21], on the same system and considering 243 barriers, we showed that, far from being constant, prefactors associated with vacancy diffusion and computed with the harmonic transition state theory (hTST) display an unexpectedly large distribution, with values that differ by up to six orders of magnitude for similar mechanisms and energy barriers. This static analysis, however, did not provide any information with respect to the impact of this broad distribution on the actual kinetics of the system, including diffusion behavior. Here, in a much more extensive simulation effort, we characterize the entropic and energetic contributions on the kinetics of a single vacancy diffusing in the same FeNiCr alloy. To do so, we use the kinetic activation-relaxation technique (KART) algorithm [22,23], an off-lattice kinetic Monte Carlo algorithm with on-the-fly catalog-building capacity, to follow vacancy diffusion over timescales close to a second and compare its behavior when using either a constant prefactor or one

computed within the hTST approximation. With more than 3 000 000 events generated, it is possible to uncover the effects of vibrational entropy on defect diffusion in these systems with sufficient statistical precision. More specifically, through the differences and similarities between these two types of simulations, we are able to determine some fundamental characteristics of CSAs through the entropic contributions taken into account by hTST, including the building of unexpected correlation that support the kinetic emergence of a Meyer-Neldel compensation law in this system [20,24–26].

II. METHODS

A. KART

Point-defect diffusion in the FeNiCr CSA is simulated with the KART [22,23,27], an off-lattice KMC method with on-the-fly event catalog building ability. This catalog is generated using the activation-relaxation technique nouveau (ARTn) [28–31], an open-ended method that samples the local energy landscape to identify saddle points present around a given minimum, irrespective of their complexity.

Local environments are characterized by their topological properties with the help of the NAUTY (No AUTomorphism, Yes?) [32]. All atoms in a sphere of a given radius around a selected atom are represented as vertices with edges added based on a distance cutoff that, here, is set between the first- and second-neighbor distance. This graph is then assigned a topological ID. This technique provides a unique identifier to the topology at the initial (IS), transition (TS), and final states, taking into account the chemical identity of the various atoms in the graph. Using the three identifiers, a unique ID is generated and attached to the atom that moves the most during an event; all atoms characterized by a specific graph are considered to have access to the same events, allowing the construction of a reusable catalog. This assumption is validated before an event is generated and a revised topology can be generated when this one-to-one relation is broken [23].

The simulated time attained by the KMC method is restricted by low barriers since the timescale of the simulation is directly dependant of the smallest barrier in the configuration. The quick oscillations between two states connected by a low barrier slow down the simulation since this flickering does not significantly contribute to the advancement of the simulation. To solve this problem, KART uses the basin-auto-constructing mean rate method (bac-MRM) [23], an extension of the mean rate method [33]. This procedure accelerates dynamical systems prone to be slowed down by low barrier events by expressing it into a set of transient and absorbing Markov chain states, from which a transition time can be obtained when observing a passage from a transient state to a specific absorbing state [34].

A more detailed description of KART can be found in Refs. [22,23,35]; only a summary of the method is presented here, along with the parameters used in this specific simulation (Fig. 1):

(1) The system is relaxed into a local energy minimum using forces computed with the Large-scale Atomic/Molecular Massively Parallel Simulator (LAMMPS) library [36].

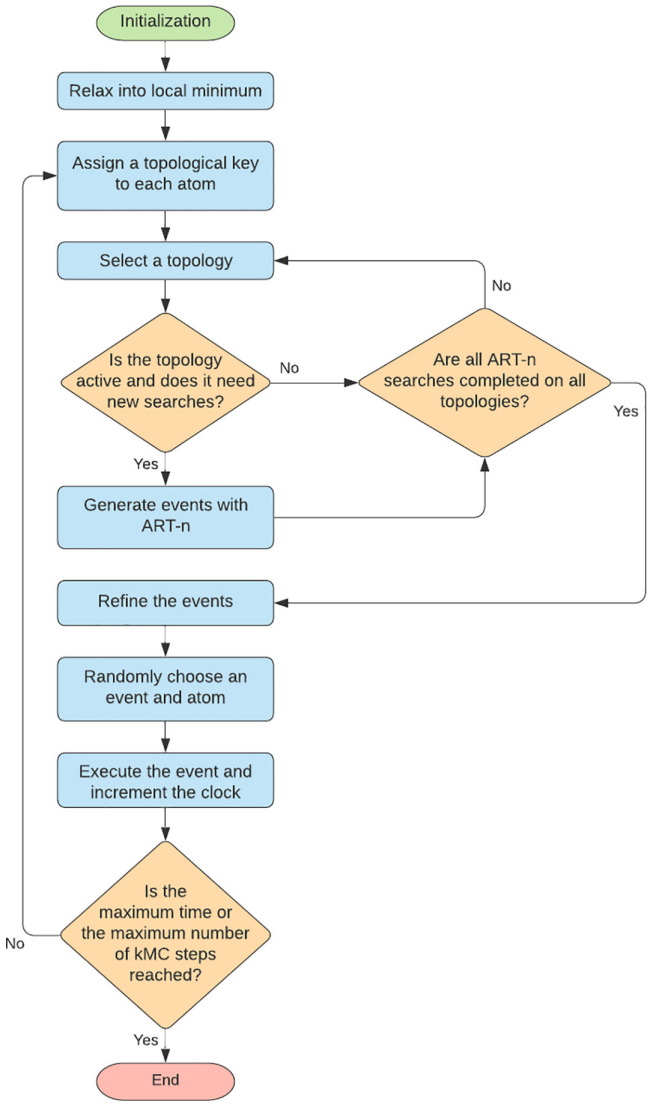

FIG. 1. Flowchart of the kinetic activation-relaxation technique. See Sec. II for more details.

(2) KART computes a connectivity graph, restricting its efforts to atoms surrounding the vacancy introduced into the system. The graph includes all atoms within 6 Å of the central atom and creates a link between those closer than 2.8 Å of each other. This graph is then sent to NAUTY [32], which returns a unique key characteristic of the automorphic group of the graph.

(3) For this simple system, if a new active topology key is found, KART launches at least 25 ARTn searches to populate the event catalog. If an active topology is already present in the catalog, new ARTn searches are launched according to the number of times it was previously seen. The number of new searches is proportional to the logarithm of the number of times the topological key has been seen. This is done to ensure the completeness of the event catalog.

For each event, a prefactor is assigned. In the standard algorithm, a fixed prefactor of 10^{13}s^{-1} is set up. Here, in half of the simulations performed, prefactors of each event are computed using hTST. Combined with the energy barriers, these serve

to produce a first evaluation of the total rate associated with moving out of the current configuration.

(4) Once the event catalog is updated to include current topologies, KART refines all the events that account for 99.99% of the total rate, meaning that it reconstructs the saddle points for these events, computes the updated prefactor, and converges it to take into account the local deformations.

(5) KART randomly selects an event with a probability proportional to its rate and executes it.

(6) The simulation clock is updated according to the refined rate of the selected event using the standard KMC Poisson distribution [37]. If the maximum simulation time or the maximum number of steps are not reached, the simulation prepares for a new step.

B. Harmonic transition state theory

For each event identified in KART, we compute the energy barrier and the transition rate Γ_{ij} between connected states i and j given by the TS theory:

$$\Gamma_{ij} = \nu \exp\left(\frac{-E}{k_B T}\right). \tag{1}$$

Here, ν is the pre-exponential factor or prefactor, E the energy barrier, calculated using the difference in energy between the IS and TS, k_B the Boltzmann constant, and T the temperature in kelvin. The prefactor ν defines the attempt frequency to reach the TS from the IS. In KMC simulations, it is usually taken as a constant value, typically around $10^{11} - 10^{13}\text{s}^{-1}$. While the exact prefactor can be obtained by thermodynamical integration [38], high-energy barriers with respect to $k_B T$ are well described using hTST.

This technique, developed by Vineyard in 1957 for systems of N atoms [39], describes the attempt frequency as the ratio of points crossing the barrier of the $3N$ dimension potential energy landscape over the total number in the IS. Within this approximation, the prefactor is given by the ratio

$$\nu_{\text{hTST}} = \frac{\prod_{i=1}^{3N} \nu_i}{\prod_{j=1}^{3N-1} \nu'_j}, \tag{2}$$

where $\nu_1 ... \nu_{3N}$ represent the vibrational frequencies at the initial minimum and $\nu'_1 ... \nu'_{3N-1}$ the frequencies at the saddle point. The product is taken over the $3N$ dimensions of the system at the IS and all frequencies but the imaginary one associated to the negative curvature at the saddle point.

As recently shown, computed prefactors can vary by several orders of magnitude between events with similar barriers in the same initial minimum [20,21].

C. Embedded atom method potential

In this paper, we use the Bonny *et al.* (Bonny-2013) embedded atom method potential [40] within its implementation in LAMMPS. This potential was developed to study aging through the formation and diffusion of radiation defects in concentrated FeNiCr ternary alloys, taking into account both the pair interactions and the embedding energy terms in the configurational energy. When tested using a Metropolis algorithm, Bonny-2013 showed that Cr segregation is energetically favored over a solid solution [21]. However, here, since diffusion takes place through vacancy-atom exchanges, Cr segregation, which also occurs through nearest-neighbor jumps from the vacancy diffusion, is very slow. As a result, this is not an issue for the vacancy-diffusion we are considering here: We check that, in the tenths of second timescale simulated here, Bonny-2013 induces no significant Cr segregation when starting from a system forming a perfect solid solution.

D. Simulated system

All simulations are performed on a 2047-atom cubic box with a length 28.4 Å and periodic boundary conditions of a 55%Fe, 28%Ni, and 17%Cr CSA, and a single vacancy at 500 K. Percentage values represent atomic composition rather than weight percents. It is built using 8×8×8 fcc unit cells of length 3.55 Å and a nearest-neighbor distance of 2.48 Å, with elements placed at random on the lattice sites, while maintaining their respective proportions. We obtain a box of FeNiCr CSA, containing 1126 atoms of Fe, 573 of Ni, and 349 of Cr, from which a vacancy is created by removing a single atom at random. The nature of the removed atom is not relevant, since the diffusion of the vacancy is governed by the local environment around it and not by the nature of the missing atom. The system is then relaxed at $T = 0$ K and $P = 0$ kPa by allowing the simulation box to adjust its size to minimize the pressure. The final volume obtained is kept fixed during the whole simulation. Given the system's size and since the system has a single vacancy and periodic boundary conditions, the simulated system is in the low-concentration limit, where no vacancy-vacancy interaction is possible, allowing the evaluation of monovacancy diffusion rates.

A total of 96 distinct simulations of around 2000 KMC steps each are performed using a constant prefactor, and 96 others with the same amount of steps using the hTST prefactor. This leads to more than 1 600 000 events generated (all events) and a total of around 190 000 KMC steps (selected events) in each case for a grand total of 3 600 000 events and 380 000 KMC steps, not including low-barrier basin events that are solved analytically. We consider all events for the characterization of the systems' energy landscape while selected events determine the systems' dynamical evolution, or their kinetics.

E. Diffusion coefficient

Point-defect diffusion in the simulated system is characterized by computing the diffusion coefficient of each element i (noted D_i). Since diffusion in a system does not depend on its previous states, we use overlapping segments of similar time intervals of around $t_f/10$ s, with t_f the total simulated time, to improve on standard deviation using Eq. (3) to compute D_i for each element i,

$$D_i = \frac{\langle R_i^2 \rangle}{6 t_{\text{int}}}, \tag{3}$$

where $\langle R_i^2 \rangle$ is the mean square displacement of element i and t_{int} is the simulated time in the interval used to compute D_i. We use here between 10 and 15 intervals depending on the total simulated time and the length of time steps. Averaging

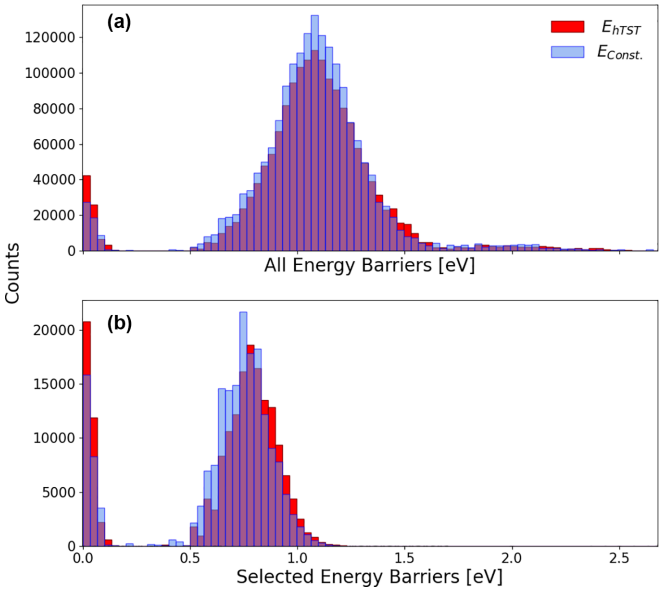

FIG. 2. (a) Distributions of all energy barriers found by ARTn in 96 KART simulations using hTST prefactors (1 662 668 events) in red and 96 others using a constant prefactor in blue (1 815 090 events). (b) Distribution of selected energy barriers for both types of simulations. Each distribution is obtained with the selected events of 96 simulations containing approximately 2000 KMC steps each, totaling around 185 000 selected events for both distributions.

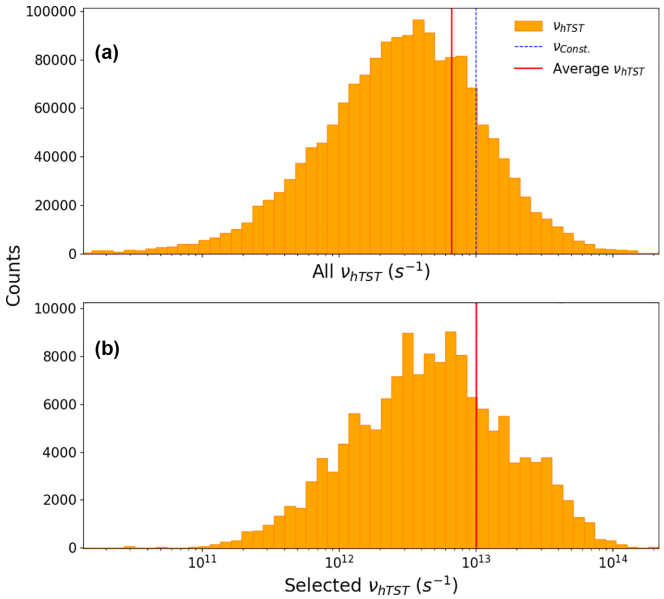

FIG. 3. (a) Distribution of the 1 662 668 observed prefactors computed with hTST found in 96 simulations. The linear average value, 6.6×10^{12} s^{-1}, is shown as a vertical dotted red line. (b) Distribution of the 180 000 selected prefactors in 96 simulations computed with hTST from events with a barrier over 0.3 eV with a linear average value of 10^{13} s^{-1} also shown with a vertical red line. For comparison, the value of the constant prefactor is also shown with a vertical blue dashed line, only in figure b, it falls directly behind the average ν_{hTST} line.

all the D_i obtained in a single simulation gives the final D_i of that simulations. These steps can also be used to obtain the vacancy diffusion coefficient (D_{vac}) if we follow the vacancy position.

III. RESULTS

A. Energy landscape observation and exploration

1. Event generation

From the 96 2000-event runs with hTST computed prefactor (hTST), a total of 1 662 668 vacancy diffusion events are generated and added to the event catalog, with an additional 1 815 090 events generated from 96 constant prefactor runs (ν_{const}). The activation barrier distributions for these two sets of events are shown in Fig. 2(a). These include the complete catalog of events generated at each step along the trajectories, whether events are selected or not in the time evolution of the trajectories. Since the energy barrier is dependent of the trajectory instead of the prefactor calculation, both distributions are similar: they show a dominant peak centered at 1.1 eV and a full width at half maximum (FWHM) of 0.41 eV for hTST and 0.37 eV for ν_{const} simulations, a width associated with the variation in local atomic environment. The FWHM is measured on a Gaussian-smoothed distribution with a bandwidth h of 0.05 eV (see Supplemental Material Fig. 1 [41]). The main peak corresponds to first-neighbor vacancy jump. Higher barriers, around 2 eV, correspond to jumps associated with atoms into the second-neighbor shell of the vacancy. A narrow peak, around 0.1 eV, is also visible in Fig. 2(a) and is associated with an extended saddle region, with a shallow minimum, found on the vacancy diffusion path for a small fraction of events. All average values are presented in Table I.

Based on the similarities observed in both energy barrier distributions of Fig. 2, we use the same maximal bac-MRM barrier threshold of 0.87 eV for both types of simulations. This relatively high basin-threshold value, that overlaps with the lower end of the energy barrier distributions, allows for an efficient handling of smaller barriers through an analytical solution, giving access to the timescale associated with jumps over higher barriers, while maintaining the correct kinetics at the cost of less details on the system's intrabasin movements.

Figure 3(a) shows the hTST prefactors associated with the event barriers of the hTST distribution in Fig. 2(a) on a semilogarithmic scale, for clarity. As expected from previous work [21], this distribution covers several orders of magnitude, ranging from 4.2×10^{7} s^{-1} to 2.3×10^{15} s^{-1}, with a FWHM that covers 1.3 orders of magnitude (see Supplemental Material Fig. 2 for details [41]). On this semilogarithmic scale, the distribution is fairly symmetric. We also compute the linearly averaged value of this distribution, as prefactors come in linearly in Eq. (1). This value is found to be 6.6×10^{12} s^{-1}, which is slightly offset from the maximum due to large prefactor values that have a greater impact on the linear average.

2. Event selection

While the structure of the energy landscape, as shown by the energy barrier distribution of generated events, appears largely independent of the type of prefactor, the time

TABLE I. Average barrier and prefactor values for simulations using the hTST approximation and for simulations using constant prefactors.

	Simulations with ν_{hTST}			Simulations with ν_{const}	
Events	Average E (eV)	Average ν_{hTST} (s^{-1})	Rate (s^{-1})	Average E (eV)	Rate (s^{-1})
All	1.11	0.66×10^{13}	4.27×10^{1}	1.10	8.17×10^{1}
Selected over 0.3 eV	0.79	1.01×10^{13}	1.09×10^{5}	0.75	2.75×10^{5}
Diffusing Fe	0.84	1.94×10^{13}	0.65×10^{5}	0.83	0.43×10^{5}
Diffusing Ni	0.78	0.82×10^{13}	1.13×10^{5}	0.76	2.18×10^{5}
Diffusion Cr	0.77	0.53×10^{13}	0.92×10^{5}	0.73	4.38×10^{5}

evolution takes place through events selected from a Poisson distribution based on their rate, a quantity that depends both on the energy barrier and the prefactor as described above. Figure 2(b) presents the energy barrier distribution for the 180 000 and 192-000 events selected each in hTST and ν_{const} runs, respectively. Similarly to Fig. 2(a), the distributions show a dominant peak, mostly associated with first-neighbor vacancy diffusion and a secondary one, around 0.1 eV, indicative of a stretched saddle region with a shallow metastable state. Knowing this, selected events under a threshold of 0.3 eV are excluded from subsequent analyses.

For hTST simulations (red), the dominant peak has an average value of 0.79 eV and a FWHM of 0.26 eV. The ν_{const} runs (blue) show a similar general aspect, but with the dominant peak shifted to lower energy barriers and slightly narrower, with an average value of 0.75 eV and a FWHM of 0.23 eV. Statistically, hTST simulations tend to favor higher energy barriers than those using ν_{const}.

hTST simulations also tend to slightly favor pathways through the extended saddle point with 20% of selected events associated with crossing the low barrier from the metastable state while these account for 15% of selected events for ν_{const} runs. Since these on-pathway events are associated with first crossing a higher-energy barrier and, therefore, have little intrinsic impact on the system kinetics, we focus our analysis on the events starting from the stable vacancy position.

To further understand the difference in specific event selection, we plot the distribution of the hTST prefactor for selected events with a barrier over 0.3 eV in Fig. 3(b). This distribution spreads over several orders of magnitude but is slightly slimmer than Fig. 3(a), with a width that covers 1.2 orders of magnitude and spans from $10^{10}\,s^{-1}$ to $4.8\times10^{14}\,s^{-1}$. The linearly computed average of selected ν_{hTST} is equal to $10^{13}\,s^{-1}$ and identical to the fixed prefactor used in ν_{const} simulations. As one might have expected, this value is slightly higher than the average prefactor for all generated events presented previously since, for a similar energy barrier, events with faster attempt frequency are kinetically favored and will be selected more often. The exact superposition of the average selected ν_{hTST} and the constant value that is generally used allows us to compare how the wide distribution in Fig. 3 affects the overall kinetics of the system, while knowing that the scale used for the constant prefactor is adequate. Once again, average barrier and prefactor values are given in Table I. As we can see, even though selected ν_{hTST} are on average equal to ν_{const}, the variation of 0.04 eV in average energy barrier results in simulation rates that are more than two times higher when employing ν_{const} due to the inversely exponential dependency in energy barriers of event rates.

B. Effects of prefactors on element selection

1. Local environment around vacancy and element selection

While the chemical composition of the alloy remains the same through the simulations, the local environment around the vacancy varies as it diffuses. Table II shows the local vacancy environment, defined as the proportion of each element in the first-neighbor shell around the point defect, averaged over all executed steps for both types of simulations. Only the 12 nearest neighbors are considered here as selected events involve only vacancy jumps to nearest-neighbor sites. Indeed, while Fig. 2 shows that jumps to the second-neighbor shell are present in the catalog, they require crossing barriers of around 2 eV, associated with characteristic times well beyond the simulated time scale covered here.

Table II shows that the average chemical distribution around the vacancy differs from the total sample composition. More specifically, for both ν_{const} and ν_{hTST}, the proportion of Fe around the missing atom is consistently lower than its alloy proportion, at 39% with ν_{const} and 38% with hTST simulations, as compared with 55% for the alloy composition. This is mostly compensated by an accrued presence of Ni, going from 28% in the bulk to 38% for constant prefactor and to 43% with the hTST prefactor in the first-neighbor shell and, to a lower degree, a slight increase of Cr presence around the vacancy, composing 17% of the alloy but representing 23% and 19% of the local environment in ν_{const} and hTST simulations, respectively. Overall, while there is a difference in the visited local environments between the two types of simulations performed, this difference remains lower than

TABLE II. Average proportion of each element around the vacancy for both types of simulations performed, compared to the total alloy composition. Each value is obtained by computing the average proportion of the 12 first neighbors around the vacancy at each step, with the standard deviation given in parenthesis.

Element	Alloy composition (%)	Environment using ν_{hTST} (%)	Environment using ν_{const} (%)
Fe	55	38 (12)	39 (13)
Ni	28	43 (12)	39 (12)
Cr	17	19 (11)	22 (12)

TABLE III. Fraction of events for which an Fe, Ni, or Cr atom is the diffusing species in hTST and constant prefactor simulations. For each simulation, the selection percentage of each element over all selected nonmetastable events with barriers over 0.3 eV is computed. These ratios are then averaged over the performed simulations in the same class, providing the standard deviation presented in parenthesis.

Element	Alloy composition (%)	Selection in ν_{hTST} simulations (%)	Selection in ν_{const} simulations (%)
Fe	55	28 (12)	16 (9)
Ni	28	28 (14)	22 (14)
Cr	17	43 (16)	62 (16)

that between all averaged visited environments and the alloy proportion, indicating that vacancy diffuses predominantly toward environments with low Fe composition due to energetic and not kinetic considerations.

It might be expected for the average selection of each atomic species to be similar to their proportion in the local environment. Surprisingly (see Table III), while Ni is overrepresented around the vacancy as it diffuses around, it is not the favored diffusing element. Even though Cr makes up for only 17% of all atoms in the system and 22% of atoms around the vacancy for ν_{const} simulations, it represents 62% of the selected atoms jumping the saddle point as the vacancy diffuses, while Fe and Ni only represent 16% and 22% of displaced atoms, respectively, as shown in Table III. Therefore Ni and, even more so, Fe atoms diffuse with a much lower probability than would be expected from their global and local concentration when using a constant prefactor.

The selection bias favoring Cr selection over the two other elements is reduced when the prefactor is computed within the hTST approximation. Even if Cr atoms are still selected more often than what would be expected according to their population (43% of selected events for a 17% global concentration), their lower selection allows a higher selection of Ni and Fe atoms. In this case, Ni is selected with a probability equal to its alloy composition (28%) and Fe atoms, while still underselected with a percentage of 28% compared to a 55% presence in the alloy, jumps with a probability much higher than with a constant prefactor.

As discussed later in this section, it is possible to explain this behavior by looking at the preferred distance between the various atomic species and the associated energy.

2. Available events per element

Vacancy diffusion is defined by the diffusion of atoms sequentially moving into the empty site. Which of the 12 atoms neighboring the vacancy jumps into this site depends on the energy barrier and associated prefactor. Figure 4 shows the broad energy barrier distribution for each of the elements. Ni atoms face, on average, higher diffusing barriers, followed by Fe and then Cr, with average barriers of 1.21 eV, 1.07 eV and 0.96 eV for hTST simulations and 1.20 eV, 1.09 eV and 0.94 eV for ν_{const} runs, respectively.

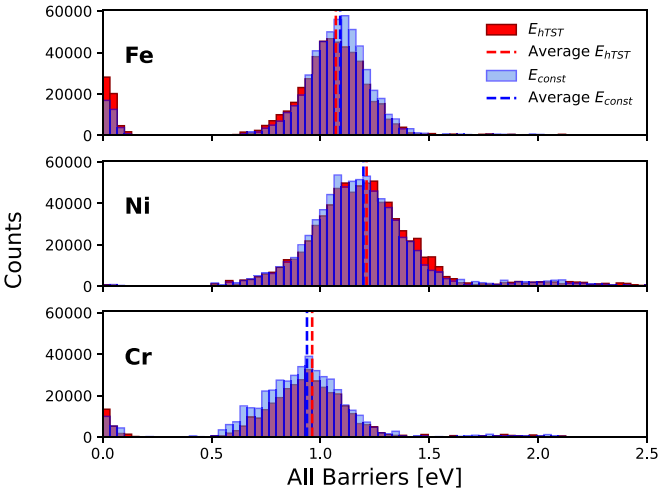

FIG. 4. Energy barrier distribution for all events separated by diffusing species for ν_{hTST} and ν_{const} simulations. Dominant peak for Fe, Ni, and Cr distributions have mean values of 1.07 eV, 1.21 eV, and 0.96 eV when using ν_{hTST} and 1.09 eV, 1.20 eV, and 0.94 eV with νconst, respectively.

Associated ν_{hTST} prefactors for these events (Fig. 5) show a different contribution to kinetics: while Fe and Ni have similar average ν_{hTST} values close to $7.1\times10^{12}\,\mathrm{s}^{-1}$, Fe's distribution is much broader, extending over more than four orders of magnitude, while Ni distribution spreads over three order of magnitude, similar to Cr, which displays the smallest average, at $4.4\times10^{12}\,\mathrm{s}^{-1}$.

The correlation between these quantities is shown in Fig. 6, where the number of counts in each bin of the distribution is given by a color coding. While there is a considerable variation in the prefactor for a given energy barrier, a linear fit on the log-linear confirms the statistical presence of a compensation factor, also called the Meyer-Neldel rule [20,25,26]. Compensation factors for Ni and Cr are small with respect to

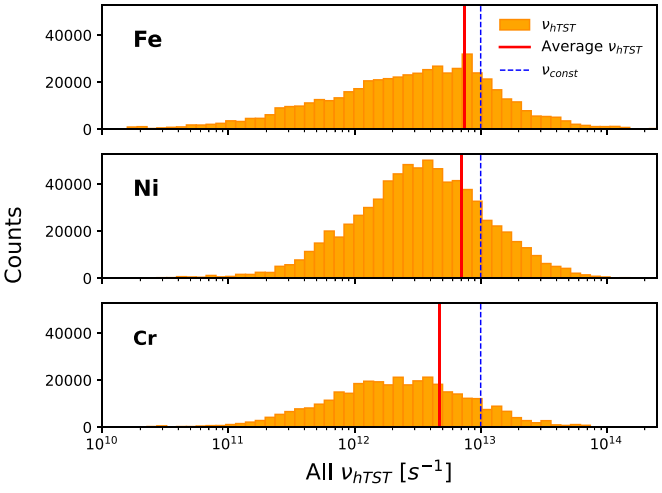

FIG. 5. HTST prefactor distribution for all events separated by diffusing species. The Fe, Ni, and Cr average hTST prefactors are shown by a red line. For reference, the set value of νconst is indicated by a blue dashed line.

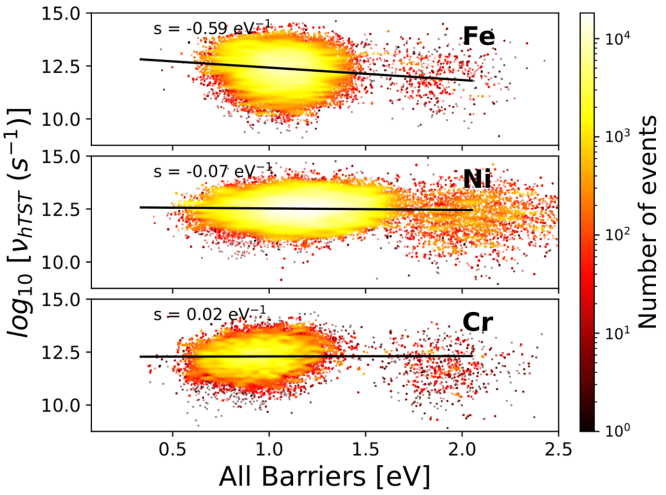

FIG. 6. Logarithmic value of all hTST prefactors observed over all simulations performed versus their associated event barriers for each element. The compensation effect is calculated separately for Fe, Ni, and Cr by using a linear fit on selected events having a barrier beyond 0.3 eV and are equal to $-0.587(0.006)\,\mathrm{eV}^{-1}$, $-0.070(0.002)\,\mathrm{eV}^{-1}$, and $0.017(0.004)\,\mathrm{eV}^{-1}$, respectively, where the numbers in parentheses indicate the standard deviation. The color map indicates the number of event in the bins for each point of the 2D distribution.

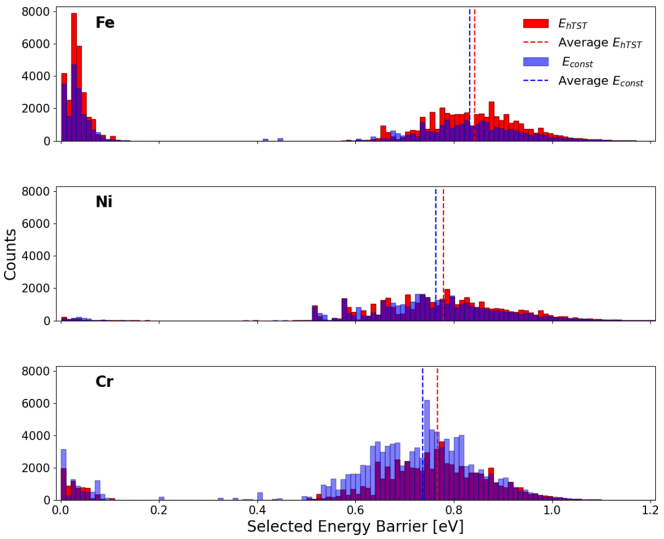

FIG. 7. Distribution of selected energy barriers separated by element for ν_{hTST} and ν_{const} simulations. Secondary peaks for Fe, Ni, and Cr have mean values of 0.84 eV, 0.78 eV, and 0.77 eV when using ν_{hTST} and 0.83 eV, 0.76 eV, and 0.73 eV with ν_{const}, respectively.

the energy scale, meaning that the average correlation between hTST prefactors and barriers is weak, with Ni showing a slightly negative slope and Cr a slightly positive one. Fe, for its part, displays a significant anticompensation correlation, with a slope equal to $-0.59\,\mathrm{eV}^{-1}$.

3. *Event selection per atomic species*

We have shown that we observe a correlation between energy barriers and prefactors in generated events. However, this correlation is not sufficient to define the diffusion kinetics as the latter is defined by selected events. Energy barrier distributions for selected events associated with Fe, Ni, and Cr jumps are shown in Fig. 7. Since the number of KMC steps is similar in both sets of simulations — with 180 000 and 192 000 executed events, respectively — the distributions are not normalized to facilitate comparison between the ν_{const} and ν_{hTST}.

The distribution of Fe barriers is similar for the two types of prefactors. When only selected event barriers with energies above 0.3 eV are considered, Fe has an average selected E_{Fe} of 0.84 eV for hTST simulations and 0.83 eV for ν_{const} simulations, higher than the average selected barrier observed when considering all atomic species together, with values of 0.79 eV for ν_{hTST} and 0.75 eV with ν_{const}. The main difference between these two distributions is in the selection frequency of Fe, with the red distribution typically having higher counts per bin. This indicates that the two types of simulations exhibit distinct evolution due to differences prefactors rather than the energy barriers.

Both distributions for Ni barriers only show a dominant peak, centered at 0.78 eV for hTST simulations and 0.76 eV for ν_{const}, with almost no metastable barriers at low energy. Other than the small difference in the average values, the two distributions display a similar aspect, both in the span covered by them and in the selection ratio of each type of simulation.

Furthermore, as expected from the high selection ratio per simulation presented above, Cr distributions have overall lower energy barrier values than Fe's and Ni's, increasing Cr's likeliness to be selected. Since ν_{const} runs are only governed by barrier height, this selection bias directly affects them, with an average Cr selected barrier of 0.73 eV, while the distribution is centered at 0.77 eV for ν_{hTST}.

Figure 7 also shows that diffusion pathways through a metastable state are much more associated with Fe jumping into the vacancy site, representing around 40% of selected events in both types of simulations, than Cr (9% of the events) and Ni (less than 3% of selected events).

Additional insights can be drawn from these distributions. First, although there are minimal variations in the shapes of the selected event distributions between the two simulation types, the average values are slightly higher with hTST, indicating that the wide hTST prefactor distribution compensates for high energy barriers, allowing them to be selected slightly more often. Second, there is a species dependence on the average energy for selected barriers. In contrast to what might be anticipated from Fig. 4, diffusing Fe crosses higher barriers than Ni, both followed by Cr. Looking at Table III, we can also see that hTST prefactors participate at least partly to the small but noticeable energy barrier difference between the diffusing species by reducing the Cr selection rate, and thus allowing Fe and Ni atoms to be selected more often.

Figure 8 presents the ν_{hTST} prefactor distribution for selected events per diffusing element, leaving aside the on-pathway metastable states with low-energy barriers. Once again, Fe has the highest average value at $1.9\times10^{13}\,\mathrm{s}^{-1}$, followed by Ni and Cr with prefactor distribution averages lower than ν_{const}, at $8.2\times10^{12}\,\mathrm{s}^{-1}$ and $5.3\times10^{12}\,\mathrm{s}^{-1}$, respectively. Despite having similar available hTST prefactors (Fig. 5) and

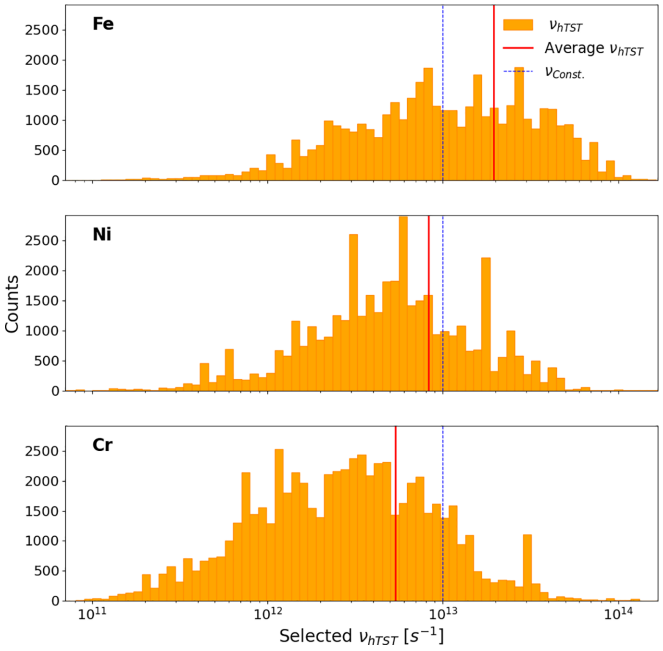

FIG. 8. Distribution of hTST prefactors for selected events with barriers over 0.3 eV separated by diffusing species. The Fe, Ni, and Cr average hTST prefactors are shown by a red dotted line and ν_{const} by a blue line. Average prefactor values are presented in Table I.

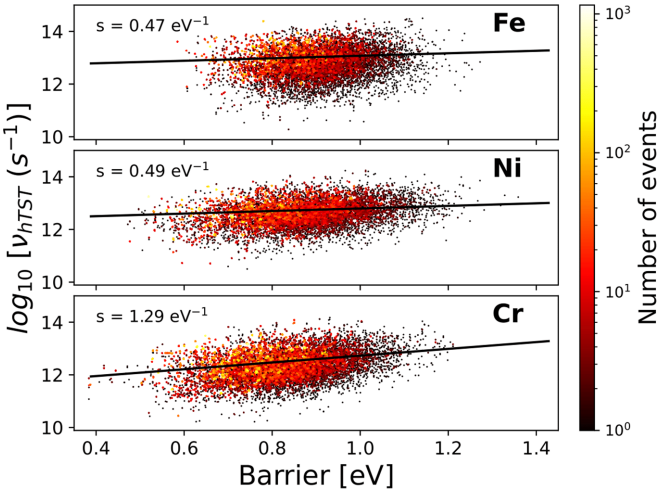

FIG. 9. Logarithmic value of selected hTST prefactors versus their associated event barriers for each element. The compensation effect is calculated separately for Fe, Ni, and Cr by using a linear fit on selected events having a barrier beyond 0.3 eV and are equal to $0.47(0.02)\,\text{eV}^{-1}$, $0.49(0.02)\,\text{eV}^{-1}$, and $1.29(0.04)\,\text{eV}^{-1}$, respectively, where the numbers in parentheses indicate the standard deviation. The color map indicates the number of event in the bins for each point of the 2D distribution.

lower barrier distribution in all available events (Fig. 4), Fe tends to diffuse through events with higher prefactors than Ni. This, combined with the fact that selected barriers are higher for Fe, indicates that high Fe barriers are correlated with higher prefactors than Ni in the range of events that are available to our simulations' timescale.

To understand the role of ν_{hTST} in the selection of diffusing species, Figs. 7 and 8 are combined in Fig. 9 to form a two-dimensional histogram in which the logarithmic value of selected hTST prefactors versus their associated barriers is given, and the number of counts in each bin is given by a color coding.

Interestingly, the compensation for Fe and Ni, despite being negative when considering all events in the catalog, becomes positive when averaged over selected events only. Moreover, both are similar in size, at $0.47(0.04)\,\text{eV}^{-1}$ and $0.49(0.02)\,\text{eV}^{-1}$, respectively, where their correlation on the full catalog differs by almost an order of magnitude. It is Cr that shows the highest correlation for selected events, at $1.29(0.02)\,\text{eV}^{-1}$.

To summarize, based on an analysis of each element's kinetics, we find that Fe displays a distribution of selected hTST prefactors with the highest values, with some as high as $10^{14}\,\text{s}^{-1}$. These high prefactor values allow the selection of higher energy barriers, compensating for their lower probability when using a constant value. Inversely, while Cr has lower selected barriers than Ni, their prefactor is also generally smaller in this low barrier end of the distribution —$5.4\times10^{12}\,\text{s}^{-1}$ vs $8.2\times10^{12}\,\text{s}^{-1}$ for Ni. This lower prefactor for a similar energy range, between 0.4 eV and 0.87 eV, which in turn makes Cr rates lower, explaining why the bias towards Cr selection is lower for hTST than ν_{const} simulations. Considering that Cr has the lowest selected barriers and the highest compensation factor, its associated prefactors are lower than for Ni and Fe, leading to average event rates, Γ_{hTST}, 4.8 times smaller than $\Gamma_{\nu\text{const}}$. Likewise, despite Ni having a higher selection rate in hTST simulations, its average barrier and prefactor values result in $\Gamma_{\nu\text{const}}$ 1.9 times higher than Γ_{hTST}. Conversely, characteristic Fe rates Γ_{hTST} are 1.5 times higher than $\Gamma_{\nu\text{const}}$.

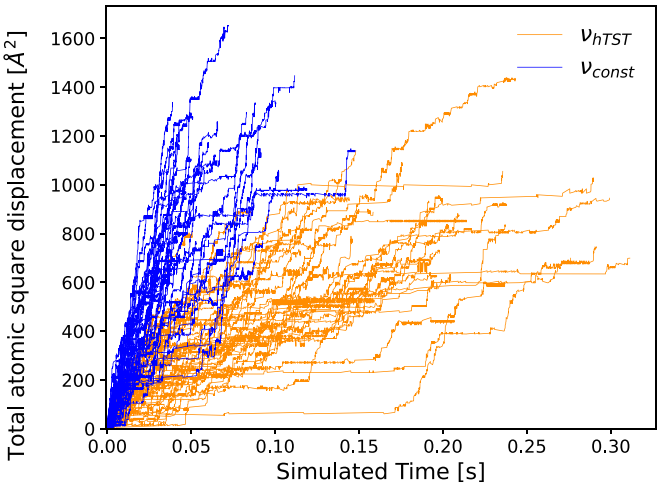

FIG. 10. Total atomic square displacement for 50 simulations using hTST prefactors and 50 others using a constant prefactor value. Total SD for hTST simulations are once again presented in red and constant ones in blue. Total SDs of the remaining simulations performed are presented in Supplemental Material Fig. 3 [41].

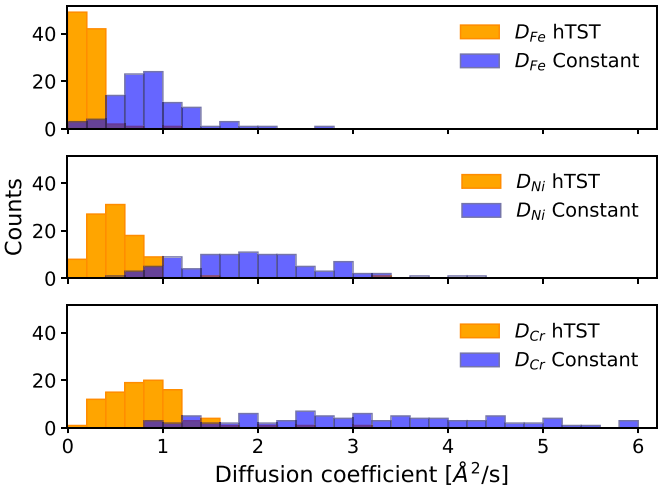

FIG. 11. Diffusion coefficients D_i at 500 K for all three elements in the alloy computed using sliding intervals for all 192 simulations. Diffusion coefficients from simulations using the hTST approximation are presented with orange bins, while the constant ones with blue bins.

C. Total square displacement and diffusion coefficients

1. Atomic displacement

Figure 10 shows the total square displacement (SD) for 50 hTST (red) and 50 constant (blue) simulations that are performed, each one having around 2000 KMC steps. Only about half of the simulations performed are shown here to make the figure more legible; similar SD trends are observed for the other half of simulations (see Supplemental Material Fig. 5). The system's kinetics is slower with hTST than with ν_{const}: constant prefactor runs require between 0.05 and 0.10 seconds to get to a total SD of 1000 Å^2, while it takes three to four times longer for hTST simulations to reach a similar displacement.

To further characterize the system's kinetics, we compute the diffusion coefficients D_i per element i for each run. The resulting distributions are presented in Fig. 11, and their mean values in Table IV. Note that the D_i values correspond to mean displacement normalized by the number of atoms of each element, giving smaller values than for the total atomic SD presented in Fig. 10.

The hTST distributions peak at relatively low diffusion coefficients and are rather narrow, rarely going above values of 1 Å^2/s. For their part, the three element D_i distributions for ν_{const} are wider and displaced to higher values, especially for the Cr distribution with D_{Cr} ranging between 1 and 6 Å^2/s.

These results are consistent with event by event analysis. Since energy barriers are lower for Cr and the local environments surrounding the vacancy are rich in this element, its diffusion is fastest, followed by Ni diffusion, and ultimately of Fe for both ν_{const} and ν_{hTST} simulations.

Even though the average selected prefactor in hTST is equal to ν_{const}, the correlation shown in Fig. 9 creates an overall slowing down of the diffusion. Contrary to what could be expected in term of the frequency of element selection, however, we see that the D_i between constant and hTST simulations is similar for all three elements, with D_{const} typically being around 3.84 times faster than D_{hTST}. This similar scaling between D_i values despite different selection ratios (Table III) indicates that Cr spends less time trapped when using hTST instead of ν_{const}. Inversely, even though with hTST, Fe shows a higher selection ratio and characteristic rate Γ_{hTST}, D_{Fe} is almost four times lower than in ν_{const} simulations, which suggests that Fe atoms tend to remain trapped in low-energy basins.

2. Vacancy displacement

Vacancy diffusion is presented in Fig. 12 for the same 50 simulations that are presented in Fig. 10, with the other half presented in annex Supplemental Material Fig. 4 [41].

There is a larger disparity in vacancy square displacement than in atomic square displacements when comparing between types of simulation.

The distribution of vacancy diffusion coefficients D_{vac} is presented in Fig. 13. D_{vac} for ν_{hTST} is equal to 925(627) Å^2/s and to 4500(2330) Å^2/s for ν_{const} simulations. As expected from the large SD values that are reached by the vacancy, D_{vac} is much greater than D_{Fe}, D_{Ni}, and D_{Cr}.

We observe D_{vac} values in ν_{const} simulations that are 4.87 times larger than D_{vac} in simulations with ν_{hTST}. This ratio is greater than the ones observed in atomic D_i, which are closer to 3.84. Therefore, even though it is possible to correct ν_{const} simulations to obtain D_i values that are similar to the correct values in hTST run by multiplying the simulated time by the $D_{\text{const}}/D_{\text{hTST}}$ ratio of 3.84 in the total atomic SD results, this correction cannot simultaneously take into account the difference in D_{vac} between simulations since $D_{\text{const}}/D_{\text{hTST}}$ ratio for the vacancy is equal to 4.87. The difference between

TABLE IV. Mean values of diffusion coefficient D at 500 K computed over sliding intervals for each element and vacancy separately using data presented in Figs. 11 and 13. The values are averaged separately over all ν_{hTST} and ν_{const} simulations, giving a single D_i and standard deviation per species i and for the vacancy.

	Simulations with ν_{hTST}		Simulations with ν_{const}		
Element	Average E (eV)	Average D (Å^2/s)	Average E (eV)	Average D (Å^2/s)	$D_{\text{const}}/D_{\text{hTST}}$
Fe	0.84	0.22 (0.13)	0.83	0.87 (0.41)	3.95
Ni	0.78	0.52 (0.37)	0.76	1.95 (0.76)	3.75
Cr	0.77	0.94 (1.04)	0.73	3.60 (1.96)	3.83
Vacancy		[9.25(6.27)]×10^2		[4.50(2.33)]×10^3	4.87

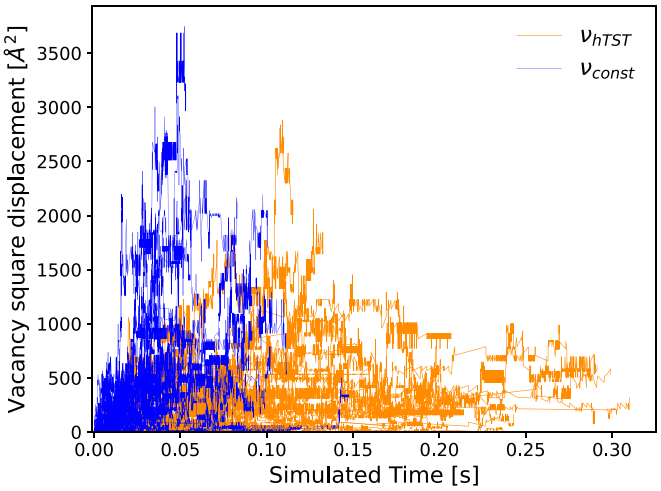

FIG. 12. Square displacement of a single vacancy in 50 simulations performed with ν_{hTST} in orange and 50 others with ν_{const} in blue. The vacancy displacements of the remaining simulations performed are presented in Supplemental Material Fig. 4 [41].

ν_{hTST} and ν_{const} simulations is therefore not simply due to an underestimated ν_{const} value. Thus, it is impossible to correctly reproduce the ν_{hTST} vacancy and atomic diffusion using a modified constant prefactor value. Values and ratios diffusion coefficients are presented in Table IV.

D. Evolution of the configurational energy

As mentioned above, we can understand the vacancy diffusion path by looking at the size of the alloyed elements as defined by their interatomic distance. These can be found in Table V with the distribution shown in Fig. 14 and with relation with the evolution of the systems' configurational energy (Fig. 15). Fe has an interatomic distance of 2.525 Å when it is next to an identical atom. Shortest pair distances are between Fe and Ni (2.494 Å) or Cr (2.490 Å), while the longest pair distance is between Ni and Cr, at 2.548 Å. Since the initial

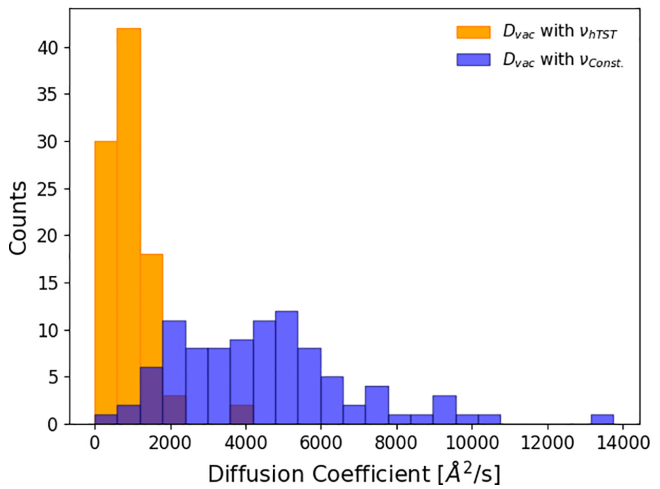

FIG. 13. Diffusion coefficient distribution for a single vacancy in a FeNiCr CSA.

TABLE V. Average distance between pair of elements obtained from the partial RDF of the whole system.

Pair	Distance (Å)
Fe-Fe	2.525
Ni-Ni	2.516
Cr-Cr	2.525
Fe-Ni	2.494
Fe-Cr	2.490
Ni-Cr	2.548

cell is a random solid solution, the local environment around the various atoms is similar to the total alloy proportion. With Fe making more than half the alloy, short distance Fe-Fe, Fe-Ni, and Fe-Cr pairs are fairly abundant, making for a more compact distribution of the elements.

As the CSA is a metastable compound [15], strain can be released as the vacancy diffuses into regions with a higher than average pressure caused by Ni-Cr interactions. Similarly to diffusion experiments, the second-long simulations generated here, while sufficient to provide information on diffusion coefficient, are not sufficient to deeply transform the compound and move it away significantly from the initial random solution. Therefore, the configurational energy remains the same and the two types of simulations therefore show similar local environments around the vacancy (Table II), with lower Fe concentration around the vacancy, compensated by a significantly higher than average Ni concentration.

Yet, entropy, through prefactor calculations, can balance out energy gains as clearly seen in Fig. 15, which presents the systems' configurational energy as a function of time as measured with respect to the initial system (set at $E = 0$ eV). Indeed, the initial configuration is a perfect solid solution, which represents a metastable local energy minimum that can relax through vacancy diffusion: it has been shown that the potential we use favors Cr clustering [21]. However, Fig. 15

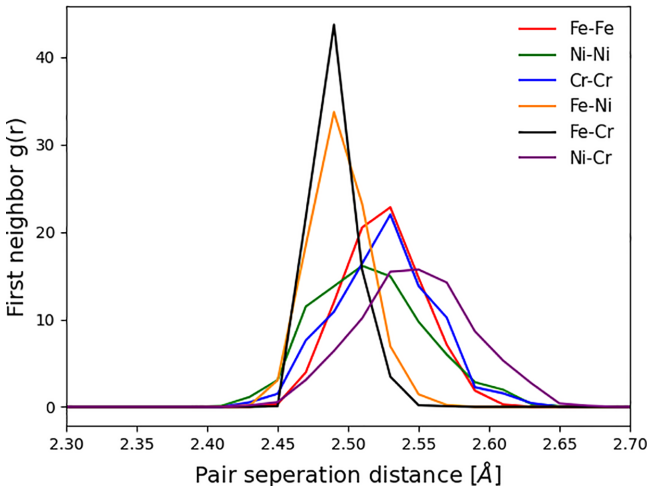

FIG. 14. First-neighbor partial RDF obtained from the bulk of whole system at a random time step. Probabilities of finding a neighbor of a certain type from another particle at a given radius r change very little between time steps, for any type of simulation.

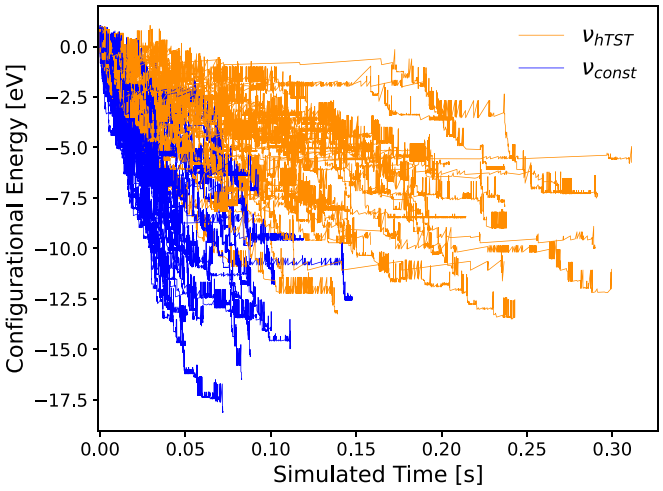

FIG. 15. Configurational energy evolution of a system containing a single vacancy for 50 simulations each for hTST and ν_{const}. These are the same simulations as in Figs. 10 and 12, with the remaining simulations presented in the Supplemental Material [41].

shows that the systems' evolution, which is controlled here by vacancy diffusion, is different for ν_{const} and ν_{hTST} simulations. For ν_{const} runs, only energy matters and vacancy diffusion lead to a significant reduction in the total energy of the systems, as preferred barriers lower the local strain. This tendency is much weaker for ν_{hTST} runs where the energy barrier is partly compensated by the vibrational entropic contribution included in the hTST prefactors. Interestingly, through a mechanism that is not fully understood, the hTST prefactors slow the systems' configurational energy relaxation by as much as 5 eV over the runs and, therefore, maintain a higher configurational entropy for the system.

IV. DISCUSSION

Previous simulation work has shown that prefactors associated with vacancy diffusion in concentrated solid solutions vary by many orders of magnitude for similar energy barriers, suggesting that this phenomenon could explain the anomalous diffusion [21]. Here, we use KART, an off-lattice KMC algorithm, to characterize the impact of this varying prefactor on the vacancy kinetics for these systems. A comparative analysis is performed between simulations that use the TS theory to compute prefactors (ν_{hTST}) and simulations that use a constant prefactor set at $10^{13}\ \text{s}^{-1}$ (ν_{const}), both for the modeling of monovacancy diffusion in a FeNiCr CSA at 500 K. This provides direct information to disentangle the role of the energy landscape and vibrational entropy in these systems. Launching 96 simulations of 2000 events with both ν_{const} and ν_{hTST}, we have generated event catalogs counting between 1 600 000 and 1 800 000 events, from which about 190 000 are selected to execute KMC steps for each type of simulation, providing a solid statistical basis for our analysis.

Generated and selected events reveal that while ν_{const} and ν_{hTST} simulations have access to roughly the same event catalog, hTST simulations tend to select energy barriers that are slightly higher, by 0.04 eV on average. This stems from the fact that, while the average selected ν_{hTST} prefactors are equal to ν_{const}, their distribution covers a large span of values, with high attempt frequencies allowing higher energy barriers to be selected. Due to their low selected barriers, ν_{const} runs show a strong bias towards Cr selections, affecting its displacement: although the Cr concentration in alloy is 17%, 62% of the total vacancy-atom exchanges performed in ν_{const} runs involve a Cr atom. This bias is reduced to 43% of the selected events when ν_{hTST} is used, as higher barriers for Fe and Ni diffusion are compensated by higher prefactors.

Barriers and hTST prefactors change according to the diffusing atom species. The barriers found here are in general agreement with the energetic order of barriers by atomic species for vacancy jumps found by *ab initio* calculations in Ref. [42], with Ni having the largest barrier, followed by Fe, then Cr. We would therefore expect Fe to diffuse faster than Ni. However, we find that this order in barriers is not maintained among the selected events, with Fe selecting higher barriers than Ni. This leads to diffusion coefficients ordered as $D_{\text{Cr}} > D_{\text{Ni}} > D_{\text{Fe}}$ in both types of simulations. A similar order is found by Jönsson for austenitic FeNiCr steels at temperatures close to 500 K [43]. Simulations of binary FeNi systems at a similar temperature by Osetsky also found D_{Fe} that are lower than D_{Ni} at certain Fe concentrations, even though pure Fe tends to diffuse faster [44]. This hierarchy between diffusion coefficients is also consistent with the rigid lattice KMC results obtained in the verification of the Bonny-2013 potential [40]. However, through tracer diffusion measurements in FeNiCr alloys, Rothman and Million obtained a higher Fe diffusion coefficient compared to Ni. Their measurements were carried out at various concentrations of Fe, Ni, and Cr, and at different temperatures ranging from 1200 to 1600 K [45,46]. While this difference could be explained by the potential used, it could also be caused by the important temperature difference between our system and theirs or the nature of the diffusing defects [47,48].

Additionally, we are able to measure vacancy diffusion, and our findings reveal that the total energy within the system dissipates through this process. Because strain affects energy barriers, the vacancy is found to diffuse preferably towards environments under compressive strain. Here, the vacancy tends to move in Fe-depleted environments as the Ni-Cr bond distance is the longest of all in this CSA. This is particularly evident in ν_{const} runs, where energy fully determines the evolution of the system. A comparison with ν_{hTST} runs demonstrates the importance of the vibrational entropy difference on the respective species' diffusion and the overall system's evolution. Such a demonstration would be difficult to make without a method such as KART.

Finally, looking at the correlation between energy barrier and prefactor, we observe a negative correlation for diffusing Fe when taking into account the full event catalog, and almost no correlation for Ni and Cr, for the same event sets. Selecting events introduces a correlation between barriers and prefactors [see Eq. (1)] and the observed relation between barriers and prefactor becomes clearly positive for events responsible for diffusion, showing the typical Meyel-Neldel compensation rule. While these observations are in agreement with recent analysis [20], clearly more analysis remains to be done to clarify the properties of the event catalog that can ensure this experimentally observed positive correlation.

V. CONCLUSION

We examine the evolution of a 55Fe-28Ni-17Cr concentrated solid solution at 500 K using either preset constant prefactors or hTST computed prefactors. Launching simulations for each case with KART, an off-lattice KMC algorithm, we generate catalogs of more than 1 600 000 events with runs of selected 2000 events (for a total of more than 180 000 selected events for each case) that reach timescales of up to 0.3 s. Comparing runs using the constant and hTST computed prefactors, we find that diffusion is slowed down with hTST prefactors. We see also that vacancy diffusion mainly takes place through atom-vacancy exchanges with Cr but that, for fairly similar barriers, the vibrational entropic difference between species, taken into account by hTST, leads to an overall decrease of the diffusion coefficients with respect to a constant prefactor set at the computed average. This suggests that vibrational entropic contributions are important for these alloys, even though disorder is largely limited to chemical.

Moreover, from the analysis of selected events, we are able to show the kinetic dependence of the compensation law. Indeed, compensation behaves differently, according to whether it is based on all the events available in the catalog or on selected ones only. This stems from the fact that the selection is governed by both the height of the barrier and the prefactor value. Thus, when prefactors are computed correctly, the selection and therefore the systems' kinetics are driven by both the configurational energy and the vibrational entropy. If any of these two quantities is increased by material properties, diffusion kinetics will be slowed down.

Building on this work, it would be interesting to further explore the impact of vibrational entropy on the other properties of CSAs as well as to validate its role directly with HEAs. While current empirical potentials are unable to provide a reasonable description of these complex systems, recent developments in machine-learning potentials would allow us to do so in the near future.

Finally, from a more fundamental side, understanding the origin of a positive kinetic compensation between prefactor and energy barriers from the overall negative correlation will also require further study on a broader range of systems.

The ARTn and kinetic ART packages as well as the data reported here are distributed freely. Please contact N.M. [49].

ACKNOWLEDGMENTS

This work was supported in part by the Materials Ageing Institute Scientific Network (MAI-SN). G.A. and C.D. acknowledge the French ANR-PRCE-HERIA project (ANR-19-CE08-0012-01) for partial support. N.M. acknowledges partial support through a Discovery grant from the Natural Science and Engineering Research Council of Canada. We are grateful to Calcul Québec and the Digital Research Alliance of Canada for generous allocation of computational resources.

[1] B. Gludovatz, A. Hohenwarter, D. Catoor, E. H. Chang, E. P. George, and R. O. Ritchie, A fracture-resistant high-entropy alloy for cryogenic applications, Science **345**, 1153 (2014).

[2] M. H. Tsai and J. W. Yeh, High-entropy alloys: A critical review, Mater. Res. Lett. **2**, 107 (2014).

[3] D. B. Miracle, J. D. Miller, O. N. Senkov, C. Woodward, M. D. Uchic, and J. Tiley, Exploration and development of high entropy alloys for structural applications, Entropy **16**, 494 (2014).

[4] M. A. Kretova, R. A. Konchakov, N. P. Kobelev, and V. A. Khonik, Point defects and their properties in the $Fe_{20}Ni_{20}Cr_{20}Co_{20}Cu_{20}$ high-entropy alloy, JETP Lett. **111**, 679 (2020).

[5] J.-W. Yeh, S.-K. Chen, S.-J. Lin, J.-Y. Gan, T.-S. Chin, T.-T. Shun, C.-H. Tsau, and S.-Y. Chang, Nanostructured high-entropy alloys with multiple principal elements: Novel alloy design concepts and outcomes, Adv. Eng. Mater. **6**, 299 (2004).

[6] A. Gali and E. P. George, Tensile properties of high- and medium-entropy alloys, Intermetallics **39**, 74 (2013).

[7] C. Li, X. Hu, T. Yang, N. K. Kumar, B. D. Wirth, and S. J. Zinkle, Neutron irradiation response of a Co-free high entropy alloy, J. Nucl. Mater. **527**, 151838 (2019).

[8] C. Lu, L. Niu, N. Chen, K. Jin, T. Yang, P. Xiu, Y. Zhang, F. Gao, H. Bei, S. Shi, M. R. He, I. M. Robertson, W. J. Weber, and L. Wang, Enhancing radiation tolerance by controlling defect mobility and migration pathways in multicomponent single-phase alloys, Nat. Commun. **7**, 13564 (2016).

[9] F. Granberg, K. Nordlund, M. W. Ullah, K. Jin, C. Lu, H. Bei, L. M. Wang, F. Djurabekova, W. J. Weber, and Y. Zhang, Mechanism of radiation damage reduction in equiatomic multicomponent single phase alloys, Phys. Rev. Lett. **116**, 135504 (2016).

[10] E. J. Pickering, A. W. Carruthers, P. J. Barron, S. C. Middleburgh, D. E. J. Armstrong, and A. S. Gandy, High-entropy alloys for advanced nuclear applications, Entropy **23**, 98 (2021).

[11] O. N. Senkov, G. B. Wilks, J. M. Scott, and D. B. Miracle, Mechanical properties of $Nb_{25}Mo_{25}Ta_{25}W_{25}$ and $V_{20}Nb_{20}Mo_{20}Ta_{20}W_{20}$ refractory high entropy alloys, Intermetallics **19**, 698 (2011).

[12] D. L. Beke and G. Erdélyi, On the diffusion in high-entropy alloys, Mater. Lett. **164**, 111 (2016).

[13] D. B. Miracle and O. N. Senkov, A critical review of high entropy alloys and related concepts, Acta Mater. **122**, 448 (2017).

[14] J. Zhang, C. Gadelmeier, S. Sen, R. Wang, X. Zhang, Y. Zhong, U. Glatzel, B. Grabowski, G. Wilde, and S. V. Divinski, Zr diffusion in BCC refractory high entropy alloys: A case of non-sluggish diffusion behavior, Acta Mater. **233**, 117970 (2022).

[15] F. Zhang, C. Zhang, S. Chen, J. Zhu, W. Cao, and U. Kattner, An understanding of high entropy alloys from phase diagram calculations, Calphad **45**, 1 (2014).

[16] S. Zhao, On the role of heterogeneity in concentrated solid-solution alloys in enhancing their irradiation resistance, J. Mater. Res. **35**, 1103 (2020).

[17] Y. Zhang, G. M. Stocks, K. Jin, C. Lu, H. Bei, B. C. Sales, L. Wang, L. K. Béland, R. E. Stoller, G. D. Samolyuk, M. Caro, A. Caro, and W. J. Weber, Influence of chemical disorder on energy dissipation and defect evolution in concentrated solid solution alloys, Nat. Commun. **6**, 8736 (2015).

[18] M. Andersen, C. Panosetti, and K. Reuter, A practical guide to surface kinetic Monte Carlo simulations, Front. Chem. **7**, 202 (2019).

[19] P. Koziatek, J. L. Barrat, P. Derlet, and D. Rodney, Inverse Meyer-Neldel behavior for activated processes in model glasses, Phys. Rev. B, **87** 224105 (2013).

[20] S. Gelin, A. C. Ruel, and N. Mousseau, Enthalpy-entropy compensation of atomic diffusion originates from softening of low frequency phonons, Nat. Commun. **11**, 3977 (2020).

[21] A. S. Lacoursière, S. Gelin, G. Adjanor, C. Domain, and N. Mousseau, Unexpected role of prefactors in defects diffusion: The case of vacancies in the 55Fe-28Ni-17Cr concentrated solid-solution alloys, Acta Mater., **237** 118153 (2022).

[22] F. El-Mellouhi, N. Mousseau, and L. J. Lewis, Kinetic activation-relaxation technique: An off-lattice self-learning kinetic Monte Carlo algorithm, Phys. Rev. B **78**, 153202 (2008).

[23] L. K. Béland, P. Brommer, F. E. Mellouhi, J. F. Joly, and N. Mousseau, Kinetic activation-relaxation technique, Phys. Rev. E **84**, 046704 (2011).

[24] R. Krug, W. Hunter, and R. Grieger, Statistical interpretation of enthalpy-entropy compensation, Nature (London) **261**, 566 (1976).

[25] S. Z. Roginskii and Y. L. Khait, The compensation effect in activation processes from the point of view of statistical kinetics, Bull. Acad. Sci. USSR **10**, 1110 (1961).

[26] A. Yelon, B. Movaghar, and R. S. Crandall, Multi-excitation entropy: Its role in thermodynamics and kinetics, Rep. Prog. Phys. **69**, 1145 (2006).

[27] M. Trochet, N. Mousseau, L. K. Béland, and G. Henkelman, Off-lattice kinetic Monte Carlo methods, in *Handbook of Materials Modeling*, edited by W. Andreoni and S. Yip (Springer, Cham, 2020), pp. 715–743.

[28] G. T. Barkema and N. Mousseau, Event-based relaxation of continuous disordered systems, Phys. Rev. Lett. **77**, 4358 (1996).

[29] R. Malek and N. Mousseau, Dynamics of Lennard-Jones clusters: A characterization of the activation-relaxation technique, Phys. Rev. E **62**, 7723 (2000).

[30] A. Jay, C. Huet, N. Salles, M. Gunde, L. Martin-Samos, N. Richard, G. Landa, V. Goiffon, S. de Gironcoli, A. Hemeryck, and N. Mousseau, Finding reaction pathways and transition states: r-ARTn and d-ARTn as an efficient and versatile alternative to string approaches, J. Chem. Theory Comput. **16**, 6726 (2020).

[31] A. Jay, M. Gunde, N. Salles, M. Poberžnik, L. Martin-Samos, N. Richard, S. de Gironcoli, N. Mousseau, and A. Hémeryck, Activation-relaxation technique: An efficient way to find minima and saddle points of potential energy surfaces, Comput. Mater. Sci. **209**, 111363 (2022).

[32] B. D. McKay and A. Piperno, Practical graph Isomorphism, II, J. Symb. Comput. **60**, 94 (2014).

[33] B. Puchala, M. L. Falk, and K. Garikipati, An energy basin finding algorithm for kinetic Monte Carlo acceleration, J. Chem. Phys. **132**, 134104 (2010).

[34] M. A. Novotny, Monte Carlo algorithms with absorbing Markov chains, Phys. Rev. Lett. **74**, 1 (1995).

[35] M. Trochet, A. Sauvé-Lacoursière, and N. Mousseau, Algorithmic developments of the kinetic activation-relaxation technique: Accessing long-time kinetics of larger and more complex systems, J. Chem. Phys. **147**, 152712 (2017).

[36] A. P. Thompson, H. M. Aktulga, R. Berger, D. S. Bolintineanu, W. M. Brown, P. S. Crozier, P. J. in t Veld, A. Kohlmeyer, S. G. Moore, T. D. Nguyen, R. Shan, M. J. Stevens, J. Tranchida, C. Trott, and S. J. Plimpton, LAMMPS: A flexible simulation tool for particle-based materials modeling at the atomic, meso, and continuum scales, Comput. Phys. Commun. **271**, 108171 (2022).

[37] N. Mousseau, P. Brommer, J. F. Joly, L. K. Béland, F. El-Mellouhi, G. K. N'Tsouaglo, O. A. Restrepo, and M. Trochet, Following atomistic kinetics on experimental timescales with the kinetic activation-relaxation technique, Comput. Mater. Sci. **100**, 111 (2015).

[38] G. Boisvert, N. Mousseau, and L. J. Lewis, Surface diffusion coefficients by thermodynamic integration: Cu on Cu(100), Phys. Rev. B **58**, 12667 (1998).

[39] G. H. Vineyard, Frequency factors and isotope effects in solid state rate processes, J. Phys. Chem. Solids **3**, 121 (1957).

[40] G. Bonny, N. Castin, and D. Terentyev, Interatomic potential for studying ageing under irradiation in stainless steels: The FeNiCr model alloy, Modell. Simul. Mater. Sci. Eng. **21**, 085004 (2013).

[41] See Supplemental Material at http://link.aps.org/supplemental/10.1103/PhysRevMaterials.8.013609 for application of Gaussian kernel density smoothing to Figs. 2 and 3 of the paper with FWHM calculations, as well as the total atomic square displacement, vacancy square displacement and total energy evolution for the 46 simulations not shown in Figs. 10, 12, and 15.

[42] S. Zhao, G. M. Stocks, and Y. Zhang, Defect energetics of concentrated solid-solution alloys from *ab initio* calculations: $Ni_{0.5}Co_{0.5}$, $Ni_{0.5}Fe_{0.5}$, $Ni_{0.8}Fe_{0.2}$, and $Ni_{0.8}Cr_{0.2}$, Phys. Chem. Chem. Phys. **18**, 24043 (2016).

[43] B. Jönsson, Assessment of the mobility of carbon in fcc C-Cr-Fe-Ni alloys, Int. J. Mater. Res. **85**, 502 (1994).

[44] Y. N. Osetsky, L. K. Béland, A. V. Barashev, and Y. Zhang, On the existence and origin of sluggish diffusion in chemically disordered concentrated alloys, Curr. Opin. Solid State Mater. Sci. **22**, 65 (2018).

[45] S. J. Rothman, L. J. Nowicki, and G. E. Murch, Self-diffusion in austenitic Fe-Cr-Ni alloys, J. Phys. F **10**, 383 (1980).

[46] B. Million, J. Růžičková, and J. Vřešťál, Diffusion in Fe-Ni-Cr alloys with an F. C. C. lattice, Mater. Sci. Eng. **72**, 85 (1985).

[47] S. Choudhury, L. Barnard, J. D. Tucker, T. R. Allen, B. D. Wirth, M. Asta, and D. Morgan, *Ab-initio* based modeling of diffusion in dilute bcc Fe–Ni and Fe–Cr alloys and implications for radiation-induced segregation, J. Nucl. Mater. **411**, 1 (2011).

[48] S. Zhao, Y. Osetsky, and Y. Zhang, Preferential diffusion in concentrated solid solution alloys: NiFe, NiCo, and NiCoCr, Acta Mater. **128**, 391 (2017).

[49] normand.mousseau@umontreal.ca.